

# A Novel Hybrid Method for Remote Sensing Image Approximation Using the Tetrolet Transform

Cuiping Shi, *Member, IEEE*, Junping Zhang, *Member, IEEE*, Hao Chen, and Ye Zhang, *Member, IEEE*

**Abstract**—Most existing image sparse approximation methods can reach their best performance only under the condition that the image has some certain properties. In addition, for the remote sensing image, it is difficult to obtain a good sparse result if it contains a lot of details. Focused on the two problems, in this paper, a novel hybrid method that is of some generality is proposed. The method exploits the advantages of the tensor product wavelet transform for representation of smooth images and the ability of the tetrolet transform to represent texture and edge effectively at the same time. Moreover, two specialized processes of decomposition are designed, which contribute to increasing the energy concentration further and preserving the information of the details as much as possible. The procedure of the proposed hybrid method is as follows: for a given remote sensing image, first, the usual tensor product wavelet transform is used, then the redundancy among adjacent wavelet coefficients is removed by making a polyphase decomposition to each subband with a  $p$ -fold filter, and after that, the approximation of the low frequency image can be obtained by reconstructing those preserved coefficients. Second, for the detailed image, the sparse decomposition is carried out by the tetrolet transform. For the high frequency subbands, an adaptive decomposition will be done for increasing the energy aggregation. After that, the approximation of the detailed image can be obtained by reconstructing those preserved coefficients. Numerical results indicate the high effectiveness of the procedure for remote sensing image sparse approximation.

**Index Terms**—Remote sensing image approximation, sparse representation, tensor product wavelet, tetrolet transform.

## I. INTRODUCTION

**I**MAGE sparse representation is to find an effective way of representation that characterizes the significant image features in a compact form. Images sparse representation is on the premise that the energy of the image should be concentrated as much as possible. Over the last years, the traditional 2-D discrete wavelet transform (2-D-DWT) as a main tool, has gained wide attention. However, the 2-D tensor product wavelet bases are suboptimal for representing geometric structures such as edges and texture. Although it can describe the horizontal and vertical

directions effectively, its support is not adapted to directional geometric properties [1]. For this reason, in the last few years, several specialized transform algorithms which aim to improve the treatment of orientated geometric image structures have been proposed, such as curvelets [2], contourlets [3], directionlets [4], and shearlets [5]. They are all nonadaptive wavelet systems, but with more directional sensitivity. Instead of choosing *a priori* basis or frame to approximate an image, one can rather adapt the approximation scheme to the image geometry [1]. In recent years, some such adaptive wavelets have been developed [6]–[9]. More recently, the grouplets [10] and the easy path wavelet transform (EPWT) [11] are proposed, which are based on finding the adaptive neighborhoods of data points and averaging them. Another kind of adaptive approach is shown in [12] and [13] which use the directional lifting-based wavelets.

In 2010, Krommweh [14] proposed the tetrolet transform for sparse image approximation, which is a kind of locally adaptive Haar wavelet transform. The tetrolet transform is almost not influenced by the Gibbs oscillation because the support region of it is very small, so it can keep the direction of the edge and texture of an image very effectively. Moreover, compared with other directional wavelets which usually focus on given geometric structure, the tetrolet transform can provide good approximations to a variety of geometric structures.

However, most of the existing image sparse approximation algorithms are not general, they can reach their best approximation performance only under the condition that the image has some certain properties. For example, the tensor product wavelet transform is optimized for presentation of smooth images, directionlets can provide the optimal approximation to cross lines, wedgelets can detect the line and surface of image effectively, and so on. Therefore, if we want to give a sparse approximation to an image, at first, we should judge whether the image is smooth or rich in details, then adopt a proper sparse approximation algorithm based on the judgment result. If the image is smooth, then the tensor product wavelet transform is adopted. If the image is rich in detailed information such as geometric characteristic, edge, and texture, then some directional wavelets can be chosen. However, it is difficult to determine whether an image is smooth or not, because it is a relative concept. A smooth image also has some detailed information, and an image which is rich in details also has a great deal of low-frequency information, so the sparse approximation algorithm that we chose by the empirical judgment may not be suitable indeed. The best way is to research a relatively common method that has a good ability of sparse approximation to any image, regardless of their characteristics.

On the other hand, compared with usual natural image, remote sensing image has its own unique characteristics. The remote

Manuscript received October 15, 2013; revised January 10, 2014; accepted April 15, 2014. Date of publication May 12, 2014; date of current version January 21, 2015. This work was supported in part by the National Natural Science Foundation of China under Grant 41301455 and Grant 61271348, in part by the 863 High Technology Program of China under Grant 2012AA12A405, and the young teachers scientific research projects of Qiqihar university under Grant 2011 k-M11. (Corresponding author: J. Zhang.)

C. Shi is with the Department of Information Engineering, Harbin Institute of Technology, Harbin 150001, China, and also with the Department of Communication Engineering, Qiqihar University, Qiqihar 161000, China (e-mail: scp1980@126.com).

J. Zhang, H. Chen, and Y. Zhang are with the Department of Information Engineering, Harbin Institute of Technology, Harbin 150001, China (e-mail: zhangjp@hit.edu.cn; hit\_hao@hit.edu.cn; zhye@hit.edu.cn).

Color versions of one or more of the figures in this paper are available online at <http://ieeexplore.ieee.org>.

Digital Object Identifier 10.1109/JSTARS.2014.2319304

sensing image usually contains a large number of ground objects, which causes the information of details is abundant, such as geometric information, edge, and texture information, even the outline of some small targets. Therefore, it is difficult to obtain a good sparse approximation for the remote sensing image because the coefficients of high frequency subbands are still very large after transformation. Thus, in order to preserve more information of details as much as possible, we have to find a way to increase the ability of energy concentration of high frequency. A reasonable way is to make a further decomposition to those high-frequency subbands in some way.

Focused on the problems that are mentioned above, in this paper, a novel hybrid method for sparse approximation is proposed. Compared with a single transform method, the proposed hybrid method has some generality. It exploits the advantages of the tensor product wavelet transform for representation of smooth images and uses the tetrolet transform for an efficient representation of edges and texture in the meanwhile. Moreover, focused on the characteristics of remote sensing image that are usually rich in details, two specialized processes of decomposition are designed, which not only benefit to increase the energy concentration further, but also can preserve more information of details at the same time. Although the idea of the proposed method is not very complicated, it can provide a good sparse performance. The results of experiments in Section V show the high effectiveness of the proposed method.

The paper is organized as follows. In Section II, the new hybrid model for sparse approximation is designed. We introduce the two stages of the design roughly, then give a brief description of the tensor-product wavelet transform and the tetrolet transform. Section III is devoted to the detailed analysis and implementation of the proposed hybrid method. Section IV mainly introduces the characteristics of image and some quality assessment measures. In Section V, we present some numerical experiments and show the high validity of the proposed hybrid method. Finally, Section VI draws the conclusions and outlines future work.

## II. HYBRID MODEL FOR IMAGE APPROXIMATION

In this paper, we propose a novel hybrid method for remote sensing image approximation. The proposed method adopts the usual tensor product wavelet transform to approximate the low frequency of the original image and uses the tetrolet transform which can give an effective representation of edges and texture to approximate the detailed image. In order to provide a better sparse approximation performance and preserve more information of details at the same time, two specialized processes of decomposition for further energy concentration are performed in two stages, respectively. The overall framework of the proposed hybrid method is shown in Fig. 1, where “HF” represents “high frequency.”

### A. Overview of the Hybrid Method

The hybrid method can be performed in two stages.

*Stage 1. Approximate the Low Frequency Image:* First, the tensor product wavelet transform is applied to the original remote sensing image. In order to remove the redundancies between adjoining wavelet coefficients localized in a same subband, we make a polyphase decomposition with a  $p$ -fold filter to each

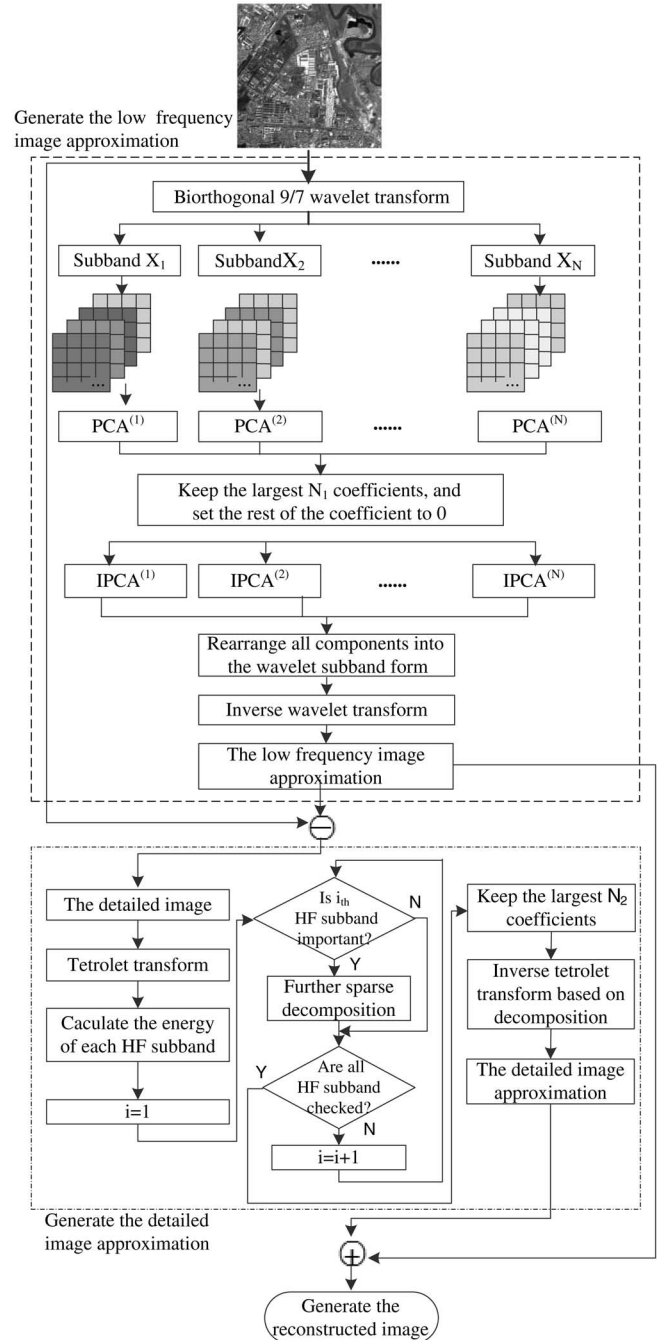


Fig. 1. Overall framework of the proposed method.

subband, and many components can be obtained. For each set of components corresponding to a subband, we calculate their own transform matrix and use the PCA to concentrate the energy. Thus, it is equivalent to concentrate the image energy twice at this stage. As a result, it can provide a better performance of sparse. Next, we apply a shrinkage procedure to preserve the  $N_1$  larger coefficients.

Finally, the inverse tensor product wavelet transform is conducted, so the approximation of the low-frequency image can be obtained.

*Stage 2. Approximate the Detailed Image:* Based on the above-mentioned results and the original remote sensing image, a detailed image that is rich in edges and texture can

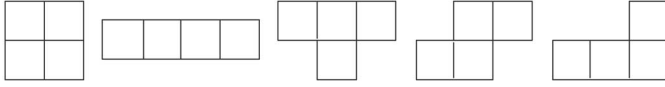


Fig. 2. Five free tetrominoes.

be obtained. At first, the image is decomposed by tetrolet transform. Following, a process of adaptive decomposition is conducted on those high-frequency subbands. In this procedure, the importance of each high-frequency subband is determined by some rule. If one subband is determined to be important, then it will be decomposed continually by tetrolet transform. The procedure of decomposition is described in detail in Section III-B. After this process, the majority coefficients of high-frequency subbands will become very small, i.e., most of the energy of the details is concentrated on a few coefficients. This is extremely beneficial to retain the information of details. Then, a shrinkage procedure is applied to preserve the  $N_2$  larger coefficients. Finally, the inverse tetrolet transform is conducted, so the approximation of the detailed image can be obtained.

Based on the approximation result of step 1) and step 2), the reconstructed image can be gained.

### B. Tensor-Product Wavelet Transform

For some applications, considering the symmetry and perfect reconstruction characteristics, two wavelets can be chosen. One is used to decompose and the other to reconstruct. This kind of wavelet is called biorthogonal wavelet for the reason that both of them must satisfy the condition of orthogonality.

For the biorthogonal wavelet, the scaling functions  $\phi(t)$  and wavelet function  $\psi(t)$  are not orthogonal. The  $\phi_{jn}(t)$  and  $\psi_{jn}(t)$  and their dual function  $\tilde{\phi}_{jn}(t)$  and  $\tilde{\psi}_{jn}(t)$  are not necessary to be biorthogonal. But, they must satisfy the conditions as follows:

$$\langle \phi_{jn}(t), \tilde{\phi}_{jn'}(t) \rangle = \delta(n - n') \quad (1)$$

$$\langle \psi_{jn}(t), \tilde{\psi}_{jn'}(t) \rangle = \delta(j - j')\delta(n - n'). \quad (2)$$

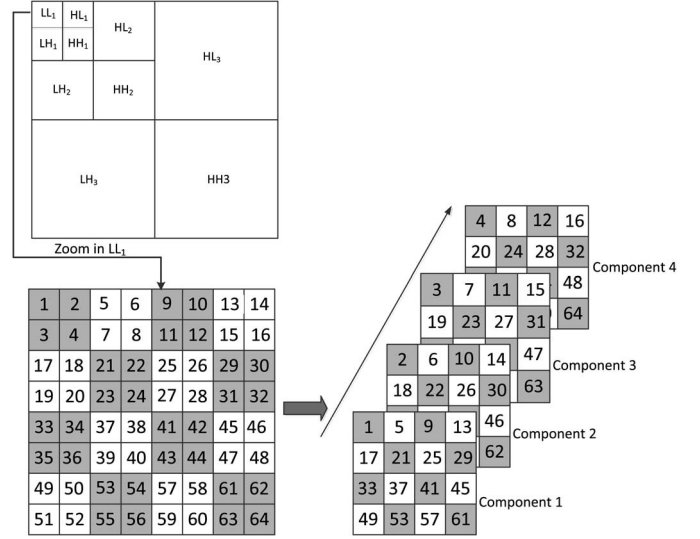
In our experiments, we use the well-known 9/7 biorthogonal filter bank.

### C. Tetrolet Transform

The concept of ‘‘Tetrominoes’’ was introduced by Golomb [15]. They are some shapes that are formed by a union of four unit squares. Without considering rotations and reflections, there are five different shapes, as shown in Fig. 2. It is obvious that each block whose size is  $N \times N$  can be covered by tetrominoes if and only if  $N$  is even.

The tetrolet transform was first proposed in [14]. The core idea of tetrolet transform is to allow more general partitions such that the local image geometry is considered, i.e., use the tetromino partitions.

The rough structure of the tetrolet transform is described as follows: for a given image, first, it should be divided into  $4 \times 4$  blocks; second, the sparse tetrolet representation in each block should be found, i.e., find the ‘‘optimal’’ partition of a block into four tetrominoes according to the geometry of the block. Third, rearrange the low-pass and high-pass coefficients of each block into a  $2 \times 2$  block, respectively. Fourth, store the high-pass

Fig. 3. Polyphase decomposition process of each subband (Take the  $LL_1$  for example).

tetrolet coefficients. Finally, for the low-pass coefficients, apply the steps that are mentioned above continually. The detailed description of the tetrolet transform is demonstrated in Section III-B.

## III. DETAILED DESCRIPTION OF THE HYBRID MODEL

Based on the overall framework in Fig. 1, for a given remote sensing image, the sparse approximation can be carried out by two stages. Stage 1 provides a sparse approximation of low-frequency image, and stage 2 provides a sparse approximation of the detailed image. In the following, we will give a detailed description of the two stages.

### A. Sparse Approximation of the Low-Frequency Image

The flowchart of this algorithm is shown in the first stage in Fig. 1. The tensor product wavelet transform is first applied to the original image, then a transform image can be obtained. However, there are still some redundancies between adjoining wavelet coefficients localized in a same subband. If we can eliminate this kind of redundancies, the energy must be further concentrated. Motivated by [16], which uses the spectral linear transforms to reduce at once the redundancies between spectral bands and the redundancies between wavelet coefficients in a same subband in hyperspectral image, we use a  $p$ -fold filter to make a polyphase decomposition to each subband and use PCA to eliminate the redundancies between components. The algorithm of the sparse decomposition of the low-frequency image is described in Algorithm 1.

Now, we give a detailed description of the polyphase decomposition process of each subband.

As described in step 2 of Algorithm 1, the polyphase decomposition process is a process that split wavelet coefficients in a subband and regroup them again. The splitting process can be realized by the  $p$ -fold filter, which divides the adjoining wavelet coefficients into successive elements. In this paper, suppose the  $p$  is 4, i.e., each subband is divided into four components. In Fig. 3,



take the decomposition of the lowest frequency subband  $LL_1$ , e.g., we give the detailed description of the polyphase decomposition process of each subband.

Suppose the size of  $LL_1$  is  $8 \times 8$ . In order to eliminate the redundancies between adjoining wavelet coefficients, the  $LL_1$  is divided into many nonoverlapping blocks whose size is  $2 \times 2$ . In Fig. 3, for visual intuitively, we use different colors to represent different blocks. The digit of each block represents the position of coefficient.

---

**Algorithm 1:** The Sparse Decomposition of the Low-Frequency Image

---

**Given:** The original image  $X = (x[i, j])_{i=1, j=1}^{M_1, M_2}$ ,  $M_1, M_2 \in \mathbb{N}$ .

**Step 1.** Suppose the  $A$  represents the 2-D tensor product wavelet transform, the result of the DWT applied to the image  $X$  is  $XA^T$ . So the transform image can be represented as:

$$XA^T := [(XA^T)^{(1)}, (XA^T)^{(2)}, \dots, (XA^T)^{(N)}].$$

Here, the  $N$  is the number of wavelet subbands.

**Step 2.** For each wavelet subband  $(XA^T)^{(i)}$ ,  $(i = 1, \dots, N)$ , make a polyphase decomposition with a  $p$ -fold filter (realized with the operator *permu*) on wavelet coefficients, then some components can be obtained. This process can be described as follows.

$$(XA^T)^{(i)} \mapsto \text{permu}(XA^T)^{(i)}.$$

The *permu* represents the procedure of splitting and regrouping wavelet coefficients of a subbands.

**Step 3.** For each component sequence of a subband, calculate the principal component transform (one per subband), and apply it to the component sequence. Suppose the  $B^{(i)}$  represents the principal component transform of the  $i$ th subband, then

$$B^{(i)}(XA^T)^{(i)} \mapsto B^{(i)}\text{permu}(XA^T)^{(i)}.$$

After the wavelet transform and the principal component transform, the transform image can be represented as  $Y$ ,

$$Y := [B^{(1)}\text{permu}(XA^T)^{(1)}, B^{(2)}\text{permu}(XA^T)^{(2)}, \dots, B^{(N)}\text{permu}(XA^T)^{(N)}]$$

$Y$  is the transform image that the energy has been concentrated twice.

**Step 4.** Make the sparse approximation to  $Y$ . For all the coefficients of the subbands of  $Y$ , preserve the larger  $N_1$  coefficients, and set the rest to 0. And we can represent the image as  $\tilde{Y}$ .

$$\tilde{Y} := [\tilde{Y}^{(1)}, \tilde{Y}^{(2)}, \dots, \tilde{Y}^{(N)}].$$


---

Now, we use the  $p$ -fold filter to make a polyphase decomposition to  $LL_1$ . First, we extract the coefficients on the top-left

corner of each block and place them according to the order of the block, so the first component is generated. Likewise, we extract the coefficients on the top-right corner of each block and generate the second component with these coefficients. The rest can be done in the same manner. Finally, the fourth component is generated by those coefficients that extracted from the lower right of each block. It can be seen from the Fig. 3 that the four adjoining wavelet coefficients in a block should be put in the same position of each component. Therefore, the redundancies between adjoining wavelet coefficients can be eliminated by applying the PCA to these components. The polyphase decomposition process of other subbands is very similar to this process, so we do not discuss them any more.

The sparse reconstruction process of the low frequency image is described in algorithm 2.

Based on the result of the algorithm 2, the approximation of the low-frequency image  $\tilde{X}_L$  is obtained. Thus, for the original image  $X$ , the detailed image  $X_d$  can be calculated by  $X_d := X - \tilde{X}_L$ .

---

**Algorithm 2:** The Sparse Reconstruction Process of the Low Frequency Image

---

**Given:** The transform image  $\tilde{Y}$ .

**Step 1.** Apply the inverse principal component transform,  $B^{(i)-1}$ ,  $(i = 1, 2, \dots, N)$  to each component sequence corresponding to a subband of  $\tilde{Y}$ . After that, the whole component sequence can be represented as

$$[B^{(1)-1}\tilde{Y}^{(1)}, B^{(2)-1}\tilde{Y}^{(2)}, \dots, B^{(N)-1}\tilde{Y}^{(N)}].$$

**Step 2.** Based on the result above, rearrange these component sequences by the inverse process of the step 2 in algorithm 1, we record the process as  $\text{permu}^{-1}$ . After the process, the inverse wavelet transform  $A^{-1}$  is applied to the transform image. Suppose the approximation of the low frequency image is  $\tilde{X}_L$ , then

$$\tilde{X}_L := [\text{permu}^{-1}(B^{(1)-1}\tilde{Y}^{(1)}), \text{permu}^{-1}(B^{(2)-1}\tilde{Y}^{(2)}), \dots, \text{permu}^{-1}(B^{(N)-1}\tilde{Y}^{(N)})]A^{-1}.$$


---

**B. Sparse Approximation of the Detailed Image**

The flowchart of this stage is shown in the second stage in Fig. 1. Based on Algorithms 1 and 2 in the Section III-A, the detailed image  $X_d$  of the original image  $X$  has been obtained. In this section, the sparse approximation of the detailed image  $X_d$  will be performed by the tetrolet transform because it can preserve the edge and texture information effectively. To solve the problem that the magnitudes of high-frequency coefficients are still very large after the tetrolet transform, we make an adaptive decomposition to those high-frequency subbands for increasing the energy concentration. The algorithm of the second stage is described as follows:

**1) Tetrolet Transform for the Detailed Image:** For the detailed image  $X_d^0 = (x_d[i, j])_{i=1, j=1}^{M_1, M_2}$ ,  $M_1, M_2 \in \mathbb{N}$ ,  $J$  is the number of

decomposition level. The  $r_{th}$  ( $r = 1, \dots, J$ ) level of the tetrolet transform is described as follows.

- 1) Divide the detailed image  $X_d^{r-1}$  into  $4 \times 4$  blocks and represent them as  $Q_{i,j}, i = 0, 1, \dots, M_1/4^r - 1, j = 0, 1, \dots, M_2/4^r - 1$
- 2) For each block, we consider the admissible tetromino coverings  $c = 1, \dots, 117$ . For each tiling  $c$ , we apply the Haar wavelet transform to the four tetromino subsets  $I_s^{(c)}, s = 0, 1, 2, 3$ . Then, the 4 low-pass coefficients  $X_d^{r,(c)}$  and 12 tetrolet coefficients  $H_l^{r,(c)}$  for each tiling are obtained

$$X_d^{r,(c)} = (x_d^{r,(c)}[s])_{s=0}^3 \quad (3)$$

$$H_l^{r,(c)} = (h_l^{r,(c)}[s])_{s=0}^3. \quad (4)$$

Here,

$$x_d^{r,(c)}[s] = \sum_{(m,n) \in I_s^C} \varepsilon[0, L(m, n)] x_d^{r-1}[m, n]$$

$$H_l^{r,(c)}[s] = \sum_{(m,n) \in I_s^C} \varepsilon[0, L(m, n)] x_d^{r-1}[m, n], l = 0, \dots, 3$$

and the  $\varepsilon[l, m], (l, m = 0, \dots, 3)$  can be obtained from the Haar wavelet transform matrix.

- 1) Choose the covering  $c^*$  that corresponding to the  $l^1$ -norm of the 12 tetrolet coefficients is minimal  

$$c^* = \arg \min_c \sum_{l=1}^3 \|H_l^{r,(c)}\|_1 = \arg \min_c \sum_{l=1}^3 \sum_{s=0}^3 |h_l^{r,(c)}[s]|.$$
- 2) Based on the last step, for each block  $Q_{i,j}$ , the optimal decomposition  $[X_d^{r,(c^*)}, H_1^{r,(c^*)}, H_2^{r,(c^*)}, H_3^{r,(c^*)}]$  can be obtained.
- 3) In order to make further decomposition using the tetrolet transform, rearrange the entries of the vectors  $X_d^{r,(c^*)}$  and  $H_l^{r,(c^*)}$  into  $2 \times 2$  matrix using a reshape function  $R$

$$X_{d|Q_{i,j}}^r = R(X_d^{r,(c^*)}) = \begin{bmatrix} x_d^{r,(c^*)}[0] & x_d^{r,(c^*)}[2] \\ x_d^{r,(c^*)}[1] & x_d^{r,(c^*)}[3] \end{bmatrix} \quad (5)$$

$$H_{l|Q_{i,j}}^r = R(H_l^{r,(c^*)}), \quad l = 1, 2, 3.$$

- 4) After finding the sparsest tetrolet representation in each block  $Q_{i,j}$ , we store the high-pass matrices and the optimum covering  $c^*$ .
- 5) Apply step 1) to step 5) to the low pass part  $X_d^{r-1}$ , until the decomposition level reaches to  $J$ .

2) *Adaptive Decomposition of High-Frequency Subbands:* For the detailed image, after the tetrolet transform, there is still a lot of useful information in high-frequency subbands due to the unique characteristics of the remote sensing image. Focusing on this problem, we calculate the energy of each high-frequency subband and judge their importance by some rule. If a high-frequency subband is judged to be important, then it will be decomposed continually by tetrolet transform. Certainly, there must be some limitations to the decomposition level of a subband. The detailed description of adaptive decomposition of high-frequency subbands is shown in Algorithm 3.

---

**Algorithm 3:** The Process of Adaptive Decomposition of High-Frequency Subbands:

---

**Given:** Suppose the high frequency subband of the transform image is  $HF_{m,d}$ ,  $m$ -Scale ( $m = 1, 2, \dots, J$ ),  $d$ -Direction ( $d = 1, 2, 3$ ). “1” represents the horizontal direction, “2” represents the vertical direction, “3” represents the diagonal direction).

**Step 1.** Calculate the energy of each  $HF_{m,d}$ , and represent it as  $E_{m,d}$ .

$$E_{m,d} = \frac{1}{MN} \sum_{i,j}^{M,N} c(i,j)^2$$

$M$  and  $N$  are the size of the corresponding subband;  $c(i,j)$  represents the coefficient of the subband that located in  $(i,j)$ .

**Step 2.** Judge each subband and decompose it if necessary.

for  $m = 1, 2, \dots, J$

- ① Calculate the average energy  $E_{m,ave}$  of the three high frequency subbands in the  $m$ th scale.

- ② For each subband of this scale, i.e.,  $HF_{m,d}(d = 1, 2, 3)$ ,

if  $E_{m,d} > E_{m,ave}$

then

the subband  $HF_{m,d}$  is judged to be important, the 1-level tetrolet transform is applied to the subband. Thus, the new four subbands of  $HF_{m,d}$  are obtained. Calculate the average energy of these new four subband and judge their importance successively. If a new subband is judged as important subband, then decompose it continually, and so on.

*Note:* the whole image at most has  $J$  layers of tetrolet decomposition, which gives the limitation to the decomposition layers of each new subband.

end

end

---

After the process of adaptive decomposition of high-frequency subbands, most of the energy of the detailed image is concentrated on a few coefficients. Then, a shrinkage procedure is conducted to preserve the  $N_2$  larger coefficients. Finally, the inverse tetrolet transform and the process of merge are applied based on the procedure in Algorithm 3. As a result, the approximation of the detailed image is obtained. It is represented as  $\tilde{X}_d$ . The  $\tilde{X}_d$  contains most of the edge and texture information.

Based on the result mentioned above, the approximation image  $\tilde{X}$  of the original image  $X$  can be represented as  $\tilde{X} := \tilde{X}_L + \tilde{X}_d$ .

Now, an example of the Algorithm 3 is given. Here, we just give a brief schematic diagram of the high-frequency subband decomposition, and some parameters such as the size of the original image and the number of preserved coefficients are not discussed in detail. The specific experiments are presented in Section V.

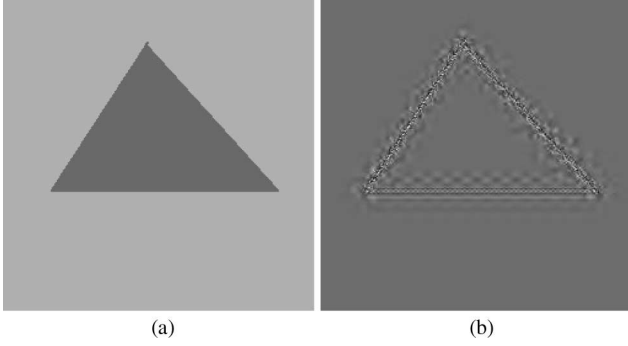


Fig. 4. Images that are used to explain the process of high-frequency subband decomposition. (a) Original image. (b) Detailed image of the original image.

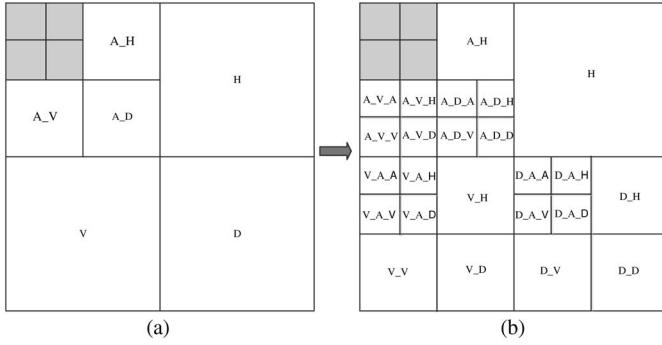


Fig. 5. Result of decomposition of the detailed image. (a) Result of decomposition after the tetrolet transform. (b) Result of adaptive decomposition of high-frequency subband to (a).

In Fig. 4(a), we give an original image  $X$ . Based on Algorithms 1 and 2, the approximation of the low-frequency image  $\tilde{X}_L$  can be obtained. Then, the detailed image  $X_d$  can be calculated by  $X_d := X - \tilde{X}_L$ . The detailed image is shown in Fig. 4(b). It is important to note that, in this paper, the detailed image is the difference of the original image and the approximation of the low-frequency image, and it can be regarded as “error image.” We should not confuse the “error image” with the image that reconstructed by some coefficients of high frequency subbands directly.

Suppose the decomposition level  $J$  is 3, after the tetrolet transform, the decomposing result of the detailed image is shown in Fig. 5(a). Here, A represents the approximated image. H represents the high frequency of the horizontal direction. V represents the high frequency of vertical direction. D represents the high frequency of diagonal direction. The energy of corresponding subbands are shown in Table I. The “Sub” in Table I represents the “subband”. Based on the process that is described in Algorithm 3 and the energy in Table I, the important high-frequency subbands in Fig. 5(a) will be decomposed continually. Take the 1-level subbands, e.g., the average energy of H, V, and D is 5.4807, and the energy of V and D are all greater than the average energy, so they are judged as important subbands and continue to be decomposed, respectively. For V, after the tetrolet transform, the average energy of V\_A, V\_H, V\_V, and V\_D is 5.6525, then V\_A is judged as important subband and continue to be decomposed. For D, after the tetrolet transform, the average energy of D\_A, D\_H, D\_V, and D\_D is 5.6068, so D\_A is judged as important subband and continue to be decomposed. Similarly,

TABLE I  
ENERGY OF EACH SUBBAND OF THE TRANSFORMED IMAGE

Sub	Energy	Sub	Energy	Sub	Energy	Sub	Energy
A	27.5301	A_A	57.4080	V_A	10.0728	D_A	10.7436
H	5.1827	A_H	12.9504	V_H	3.0078	D_H	3.7615
V	5.6525	A_V	20.5780	V_V	5.5875	D_V	4.0598
D	5.6068	A_D	19.1839	V_D	3.9420	D_D	3.8623

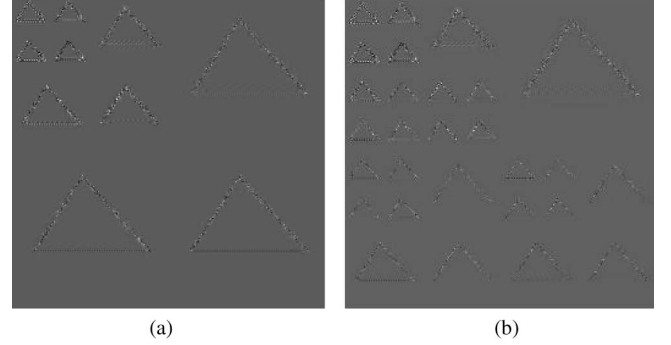


Fig. 6. Transform images that are corresponding to Fig. 5. (a) Transform image after the tetrolet transform. (b) Transform image after the process of adaptive decomposition of high-frequency subbands.

other subbands are decomposed in this way. Finally, the result of decomposition is shown in Fig. 5(b). The transform images that corresponding to Fig. 5 are shown in Fig. 6.

#### IV. IMAGE CHARACTERISTICS AND QUALITY EVALUATION

Suppose  $X$  and  $Y$  represent the original image and the reconstructed image, the  $M$  and  $N$  represent the number of rows and columns, respectively. In this section, the characteristic of the image is analyzed first, then some evaluation indices of image quality are given from the objective and subjective perspective.

##### A. Characteristics of Image

The characteristic of the spatial domain of an image can be described by spatial frequency measure (SFM) [17]. The SFM is defined as follows:

$$SFM = \sqrt{(R)^2 + (C)^2}. \quad (6)$$

Here,

$$C = \sqrt{\frac{1}{MN} \sum_{j=1, i=2}^{N, M} [x(i, j) - x(i-1, j)]^2}$$

and

$$R = \sqrt{\frac{1}{MN} \sum_{i=1, j=2}^{M, N} [x(i, j) - x(i, j-1)]^2}$$

where  $R$  represents the row frequency,  $C$  represents the column frequency, and  $x(i, j)$  represents the pixel of the image. SFM indicates the total frequency of an image, which represents the extent that an image rich in details. The more details that an image contains, the larger the value of SFM is. In this paper, SFM is used to analyze the influence of the details to the sparse approximation.

### B. Quality Assessment Measure

Most of the literatures adopt the peak-signal-to-noise-ratio (PSNR) or MSE to evaluate the quality of the reconstructed image. However, they have been proved to be inconsistent with the human eye perception [18]. Sometimes, the visual effect is not very good even if the PSNR of the reconstructed image is high. In order to give a comprehensive evaluation of the quality of reconstructed image, we choose PSNR, root mean square error (RMSE), maximum absolute difference (MAD), and mean absolute error (MAE) as objective evaluation indices, and in addition, we adopt structural similarity index measure (SSIM) [17] as the subjective evaluation index.

1) *Objective Evaluation Index*: The PSNR can be calculated by

$$PSNR = 10\log_2 \frac{L^2}{\|f - \hat{f}\|_2^2} \quad (7)$$

where  $L$  is the possible maximum value of the image, and  $f$  and  $\hat{f}$  are the original image and the reconstructed image, respectively.

The RMSE can be calculated as follows:

$$RMSE = \sqrt{\frac{1}{MN} \sum_{x,y} e(x,y)^2} \quad (8)$$

where  $e(x,y)$  means the error of the  $f$  and  $\hat{f}$ .

The MAD can be represented as

$$MAD = \max_{x,y} \{|e(x,y)|\}. \quad (9)$$

The MAE is determined by

$$MAE = \frac{1}{MN} \sum_{x,y} |e(x,y)|. \quad (10)$$

2) *Subjective Evaluation Index*: The SSIM is a method for measuring the similarity between two images. It can be calculated as follows:

$$SSIM(X,Y) = \frac{2\mu_X\mu_Y + c_1}{\mu_X^2 + \mu_Y^2 + c_1} \cdot \frac{2\sigma_X\sigma_Y + c_2}{\sigma_X^2 + \sigma_Y^2 + c_2} \cdot \frac{\sigma_{XY} + c_3}{\sigma_X\sigma_Y + c_3} \quad (11)$$

where  $\mu_X$  and  $\mu_Y$  represent the average of  $X$  and  $Y$ , respectively.  $\sigma_X$  and  $\sigma_Y$  represent the standard variance of  $X$  and  $Y$ , respectively.  $\sigma_{XY}$  represents the covariance of  $X$  and  $Y$ .  $c_1 = (k_1L)^2$ ,  $c_2 = (k_2L)^2$ ,  $c_3 = c_2/2$ ,  $k_1 = 0.001$ ,  $k_2 = 0.002$  (default), and  $L$  is the dynamic range of pixel value.

The range of the SSIM is  $[-1, 1]$ . The value of SSIM is larger, which means the reconstructed image is closer to the original image from the visual perspective. When the SSIM equals to 1, it means the reconstructed image and the original image is exactly the same.

## V. EXPERIMENT AND RESULTS

In this section, some experiments are implemented to testify the performance of the proposed hybrid method. We apply the

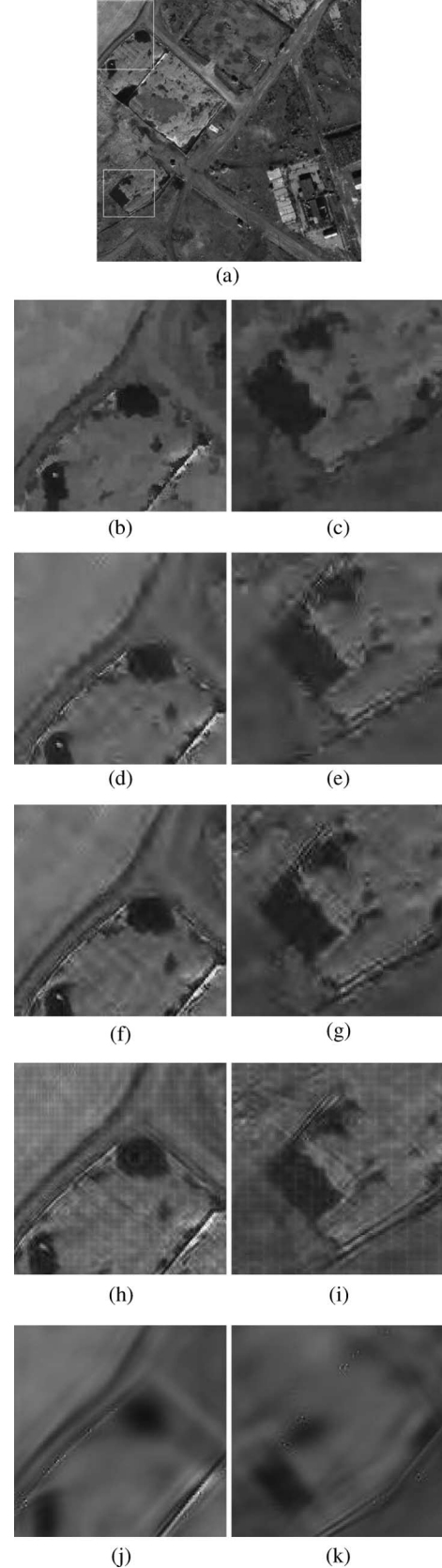


Fig. 7. PSNR and the local amplification image of the reconstructed image obtained by different methods. (a) Original remote sensing image. (b) and (c) Tensor product 9/7 wavelet transform, PSNR = 25.09. (d) and (e) Tetrolet transform, PSNR = 25.49. (f) and (g) Proposed hybrid method, PSNR = 26.32. (h) and (i) Contourlet transform, PSNR = 24.18. (j) and (k) Curvelet transform, PSNR = 22.38.



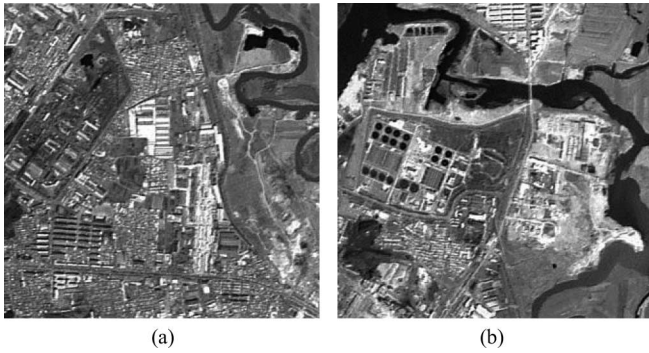


Fig. 8. Two remote sensing images that are used as test images. (a) RS1. (b) RS2.

TABLE II  
COMPARISON OF THE PROPOSED HYBRID METHOD AND OTHER FOUR METHODS FOR PSNR ( $N_1 : N_2 = 4 : 1$ )

Image	$N_1$	$N_2$	9/7 PSNR	Tetrolet PSNR	Curvelet PSNR	Contourlet PSNR	Hybrid PSNR
RS1	4000	1000	20.27	20.23	17.42	19.42	<b>21.70</b>
	6000	1500	21.39	21.94	17.86	20.34	<b>22.63</b>
	8000	2000	22.30	22.99	18.23	21.13	<b>23.45</b>
RS2	4000	1000	21.60	21.34	17.91	20.42	<b>23.01</b>
	6000	1500	22.87	23.23	18.48	21.49	<b>24.11</b>
	8000	2000	23.86	24.35	18.94	22.35	<b>24.95</b>

TABLE III  
COMPARISON OF THE PROPOSED HYBRID METHOD AND OTHER FOUR METHODS FOR PSNR ( $N_1 : N_2 = 3 : 1$ )

Image	$N_1$	$N_2$	9/7 PSNR	Tetrolet PSNR	Curvelet PSNR	Contourlet PSNR	Hybrid PSNR
RS1	3000	1000	19.73	18.48	17.20	18.95	<b>21.16</b>
	6000	2000	21.59	22.18	17.94	20.51	<b>22.71</b>
	9000	3000	22.93	23.64	18.49	21.68	<b>23.90</b>
RS2	3000	1000	20.96	19.88	17.64	19.87	<b>22.44</b>
	6000	2000	23.08	23.49	18.58	21.68	<b>24.19</b>
	9000	3000	24.53	25.03	19.26	22.92	<b>25.36</b>

hybrid method to several remote sensing images and compare it with the 9/7 tensor product wavelet transform and the tetrolet transform. In addition, two directional wavelet transform, i.e., the curvelet transform [2] and the contourlet transform [3], are considered to further prove the validity of the proposed method. The MATLAB toolbox of curvelet and contourlet we used are downloaded from [19] and [20], respectively. All the size of the test image set is  $512 \times 512$  (262 144 coefficients).

First, the original remote sensing image is given in Fig. 7(a). For the proposed hybrid method, in the process of sparse approximation of the low-frequency image, we adopt the five levels of the 9/7-biorthogonal tensor product filter bank and apply a shrinkage procedure to keep 6000 coefficients. Then, in the process of sparse approximation of the detailed image, we apply the five levels of tetrolet transform and keep 1500 coefficients. Subsequently, for comparison, we make a sparse representation of the original image using the 9/7-biorthogonal tensor conduct wavelet transform, the tetrolet transform, curvelet transform, and contourlet transform under the same condition. The four transform methods are keeping 7500 coefficients directly during the shrinking procedure. The PSNR and the local amplification

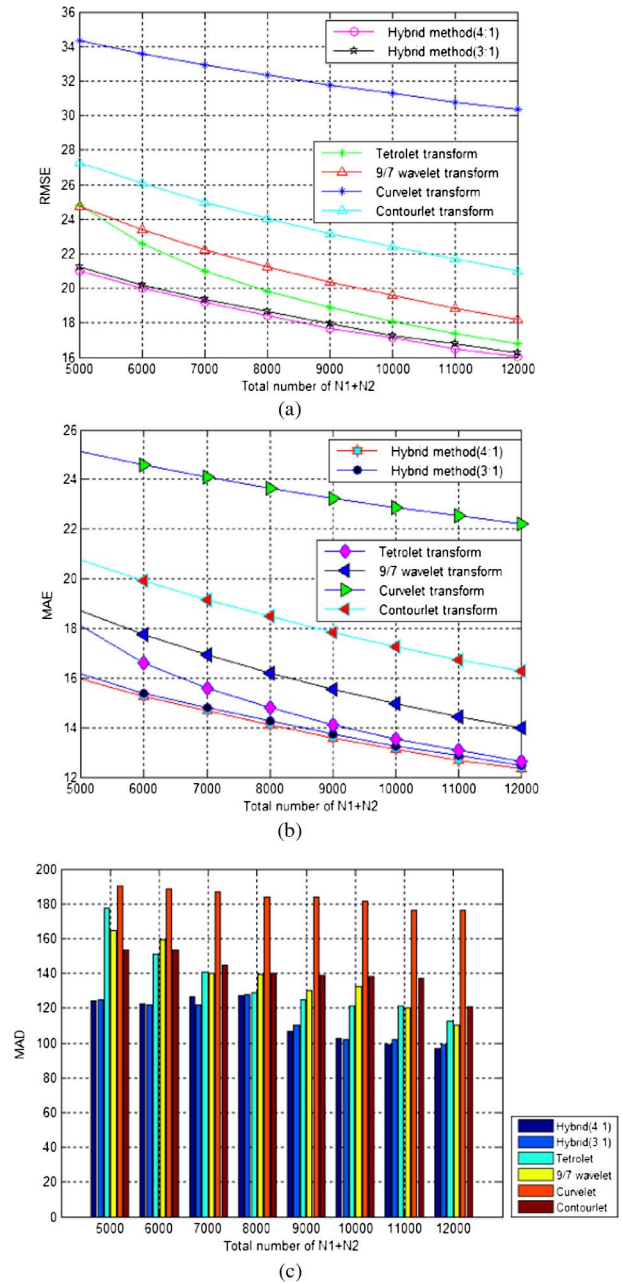


Fig. 9. Result of some objective evaluation indices under the condition that  $N_1 : N_2 = 4 : 1$  and  $N_1 : N_2 = 3 : 1$ . (a) Result of the RMSE. (b) Result of the MAE. (c) Result of the MAD.

image of the reconstructed image obtained by different methods are shown in Fig. 7. It can be seen from Fig. 7 that the proposed method is of best performance, the effect of the tetrolet transform is slightly lower, and the result of the curvelet is the worst.

In order to further confirm the effectiveness of the proposed scheme, we choose the other two remote sensing images as the test image, which are named as “RS1” and “RS2,” respectively. They are shown in Fig. 8. Likewise, the decomposition level is five. In the proposed hybrid method, we keep  $N_1$  coefficients to appropriate the low-frequency image and keep  $N_2$  coefficients to appropriate the detailed image. Then, we compare the proposed method with the other four transform methods that use  $N_1 + N_2$  coefficients directly. The experiments are implemented under the different condition that  $N_1 : N_2 = 4 : 1$  and  $N_1 : N_2 = 3 : 1$ .



TABLE IV  
COMPARISON OF THE PROPOSED HYBRID METHOD AND OTHER FOUR METHODS FOR  
SSIM ( $N_1 : N_2 = 4 : 1$ )

Image	$N_1$	$N_2$	9/7 SSIM	Tetrolet SSIM	Curvel et SSIM	Contour -let SSIM	Hybrid SSIM
RS1	4000	1000	0.657	0.694	0.332	0.600	<b>0.772</b>
	6000	1500	0.743	0.793	0.390	0.684	<b>0.822</b>
	8000	2000	0.797	0.842	0.438	0.743	<b>0.857</b>
RS2	4000	1000	0.719	0.746	0.417	0.649	<b>0.804</b>
	6000	1500	0.784	0.830	0.476	0.721	<b>0.847</b>
	8000	2000	0.826	0.866	0.523	0.767	<b>0.874</b>

TABLE V  
COMPARISON OF THE PROPOSED HYBRID METHOD AND OTHER FOUR METHODS FOR  
SSIM ( $N_1 : N_2 = 3 : 1$ )

Image	$N_1$	$N_2$	9/7 SSIM	Tetrolet SSIM	Curvel et SSIM	Contour -let SSIM	Hybrid SSIM
RS1	3000	1000	0.607	0.587	0.304	0.550	<b>0.741</b>
	6000	2000	0.755	0.806	0.400	0.697	<b>0.827</b>
	9000	3000	0.827	0.866	0.470	0.777	<b>0.876</b>
RS2	3000	1000	0.678	0.662	0.387	0.608	<b>0.780</b>
	6000	2000	0.794	0.839	0.486	0.731	<b>0.852</b>
	9000	3000	0.851	0.883	0.552	0.793	<b>0.888</b>

We evaluate the quality of the reconstructed images that is obtained by different methods from the perspective of the objective and subjective. In this paper, the PSNR, RMSE, MAD, and MAE are chosen as the objective evaluation indices and the SSIM is adopted as the subjective evaluation index. The PSNR results are tabulated in Tables II and III, respectively.

From the result of Tables II and III, it can be seen that the PSNR of the reconstructed image obtained by the proposed hybrid method is higher than that of the other four methods, whatever the ratio of  $N_1$  and  $N_2$ . It can prove the effectiveness of the proposed method. Furthermore, we make an analysis of the result and find the PSNR of RS2 is bigger than the PSNR of RS1, nearly 1.5 dB under the same condition. The complexity of the image is the main reason. Based on (6), the SFM of RS1 and RS2 are calculated. As a result, the SFM of RS1 is 28.9349 and the SFM of RS2 is 26.8928. Based on the previous analysis in Section IV-A, the more detail information that an image contains, the SFM of it is larger, i.e., compared with RS1, the RS2 has less detail information, which makes it concentrate the energy more easily. In other words, it can be sparsed more effectively. Thus, we can draw a conclusion that the proposed hybrid method is very effective, and its advantage gets more obvious when the complexity of the remote sensing image is low relatively.

Now, we take the RS1, e.g., evaluate the quality of reconstructed images that is obtained by different methods using the RMSE, MAE, and MAD. Under the condition that  $N_1 : N_2 = 4 : 1$  and  $N_1 : N_2 = 3 : 1$ , the results are shown in Fig. 9.

It can be seen from the Fig. 9 that the RMSE, MAE, and the MAD of the reconstructed image obtained by the proposed hybrid method are all smaller than that of the other transform methods, whatever the ratio of  $N_1$  and  $N_2$ . Thus, it can prove the validity of the proposed method. For the hybrid method, the result obtained on the condition that  $N_1 : N_2 = 4 : 1$  is slightly better than that in the condition when  $N_1 : N_2 = 3 : 1$ .

For another remote sensing image RS2, the conclusion is very similar to that of RS1, so we will not discuss it any more.

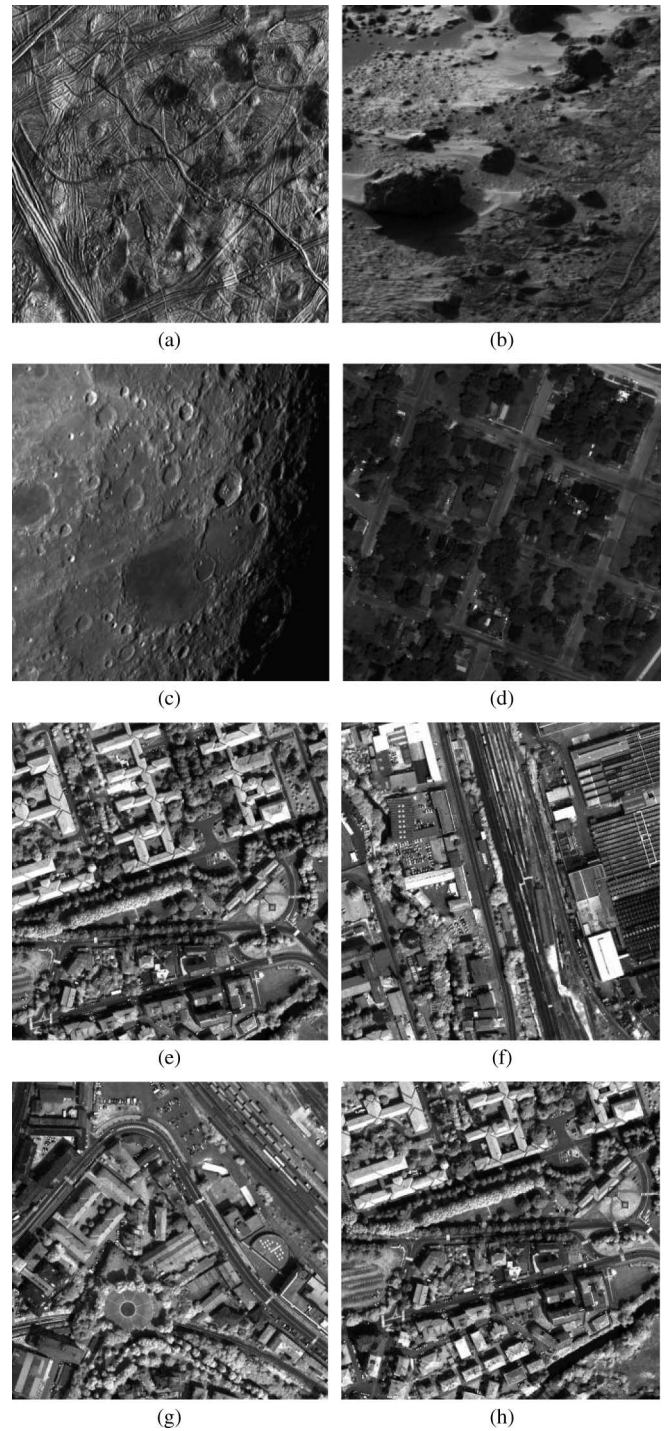


Fig. 10. Test remote sensing image set used in the experiment. The size of these images is  $512 \times 512$  and bit depth is 8. (a) Europa3. (b) Marstest. (c) Lunar. (d) Houston. (e) Pavia-1. (f) Pavia-2. (g) Pavia-3. (h) Pavia-4.

Now, from the perspective of the subjective, we evaluate the quality of reconstruction image under the condition that  $N_1 : N_2 = 4 : 1$  and  $N_1 : N_2 = 3 : 1$ , respectively. The SSIM results are tabulated in Tables IV and V.

Tables IV and V have demonstrate that, from the perspective of the subjective, the effect of the reconstructed image that obtained by the proposed hybrid method is superior to that obtained by the other four methods obviously.

TABLE VI  
SFM OF THE IMAGES OF THE LARGER TEST IMAGE SET

Image	Europa3	Marstest	Lunar	Houston
SFM	57.96	14.86	23.39	18.46
Image	Pavia-1	Pavia-2	Pavia-3	Pavia-4
SFM	50.77	57.64	51.09	51.16

TABLE VII  
COMPARISON OF THE PROPOSED METHOD AND OTHER TRANSFORM-BASED METHODS  
( $N_1 + N_2 = 8000$ )

Image	Algorithm	PSNR	RMSE	MAE	MAD	SSIM
Europa3	9/7	19.20	27.97	21.84	140.06	0.675
	Tetrolet	19.65	26.56	20.56	158.22	0.729
	Curvelet	17.17	35.34	27.69	179.80	0.366
	Contourlet	19.02	28.53	22.37	158.01	0.659
	Hybrid (4:1)	<b>20.29</b>	<b>24.66</b>	<b>19.29</b>	<b>132.62</b>	<b>0.773</b>
	Hybrid (3:1)	<b>20.21</b>	<b>24.90</b>	<b>19.47</b>	<b>134.06</b>	<b>0.768</b>
Marstest	9/7	27.00	11.39	8.62	70.10	0.851
	Tetrolet	27.39	10.89	8.07	77.57	0.867
	Curvelet	22.43	19.27	14.43	104.42	0.539
	Contourlet	25.60	13.38	10.31	89.48	0.793
	Hybrid (4:1)	<b>28.31</b>	<b>9.80</b>	<b>7.34</b>	<b>60.27</b>	<b>0.903</b>
	Hybrid (3:1)	<b>28.20</b>	<b>9.92</b>	<b>7.42</b>	<b>60.32</b>	<b>0.901</b>
Lunar	9/7	28.08	10.06	7.24	64.92	0.847
	Tetrolet	28.26	9.86	7.12	73.18	0.814
	Curvelet	23.36	17.32	11.87	137.13	0.553
	Contourlet	26.10	12.64	9.48	106.95	0.754
	Hybrid (4:1)	<b>29.11</b>	<b>8.93</b>	<b>6.41</b>	<b>79.00</b>	<b>0.889</b>
	Hybrid (3:1)	<b>28.97</b>	<b>9.08</b>	<b>6.50</b>	<b>79.34</b>	<b>0.886</b>
Houston	9/7	28.71	9.36	7.07	80.63	0.846
	Tetrolet	29.17	8.88	6.60	76.56	0.869
	Curvelet	24.41	15.35	10.83	192.18	0.581
	Contourlet	27.34	10.95	8.21	140.36	0.798
	Hybrid (4:1)	<b>29.34</b>	<b>8.70</b>	<b>6.54</b>	<b>76.88</b>	<b>0.879</b>
	Hybrid (3:1)	<b>29.27</b>	<b>8.77</b>	<b>6.58</b>	<b>68.21</b>	<b>0.878</b>
Pavia-1	9/7	19.38	27.40	20.78	170.91	0.820
	Tetrolet	20.05	25.31	19.63	196.68	0.862
	Curvelet	16.01	40.37	31.11	228.41	0.493
	Contourlet	18.62	29.90	22.69	231.19	0.787
	Hybrid (4:1)	<b>20.17</b>	<b>25.01</b>	<b>18.93</b>	<b>179.33</b>	<b>0.869</b>
	Hybrid (3:1)	<b>20.10</b>	<b>25.22</b>	<b>19.06</b>	<b>184.34</b>	<b>0.868</b>
Pavia-2	9/7	19.14	28.16	21.22	186.18	0.769
	Tetrolet	19.55	26.85	19.71	217.45	0.808
	Curvelet	16.33	38.93	29.30	221.30	0.483
	Contourlet	18.31	30.99	23.44	214.73	0.729
	Hybrid (4:1)	<b>19.85</b>	<b>25.95</b>	<b>19.57</b>	<b>178.47</b>	<b>0.829</b>
	Hybrid (3:1)	<b>19.77</b>	<b>26.18</b>	<b>19.65</b>	<b>179.79</b>	<b>0.826</b>
Pavia-3	9/7	19.73	26.30	19.70	166.07	0.774
	Tetrolet	20.25	24.32	18.85	181.24	0.821
	Curvelet	16.79	36.89	27.46	203.17	0.480
	Contourlet	19.10	28.29	21.23	199.58	0.747
	Hybrid (4:1)	<b>20.53</b>	<b>24.00</b>	<b>18.02</b>	<b>161.41</b>	<b>0.833</b>
	Hybrid (3:1)	<b>20.41</b>	<b>24.25</b>	<b>18.25</b>	<b>168.00</b>	<b>0.831</b>
Pavia-4	9/7	19.35	27.47	20.77	196.06	0.819
	Tetrolet	20.09	25.25	18.68	222.35	0.859
	Curvelet	16.02	40.32	30.81	224.29	0.497
	Contourlet	18.56	30.10	22.74	218.22	0.785
	Hybrid (4:1)	<b>20.18</b>	<b>24.97</b>	<b>18.51</b>	<b>172.67</b>	<b>0.869</b>
	Hybrid (3:1)	<b>20.13</b>	<b>25.18</b>	<b>18.59</b>	<b>172.29</b>	<b>0.867</b>

Ratio inside the bracket represents  $N_1 : N_2$ .

A much larger test image set is chosen in order to further prove the validity of the proposed method. Part of the test images come from CCSDS reference test image set, whose images we used include “Europa3” with size of  $600 \times 557$ , “Marstest” and “Lunar” with size of  $512 \times 512$ . We crop the upper left of the “Europa3” with size of  $512 \times 512$  for comparison under the

same condition. The “Houston” is acquired by the WorldView-2 Sensor over Houston, TX, USA. The “Pavia-1,” “Pavia-2,” “Pavia-3,” and “Pavia-4” are acquired by the QuickBird Sensor over Pavia, northern Italy. The test image set is shown in Fig. 10. Table VI lists the SFM of these images. Based on the analysis in Section IV-A, most of these images are rich in details.

The experiments are implemented under the condition that the level of decomposition is five and the total number of the preserved coefficients is 8000. The comparison result of the proposed hybrid method and other transform-based methods are tabulated in Table VII. These results prove the high effectiveness of the hybrid method for remote sensing image approximation once again, no matter from the subjective or objective perspective.

## VI. CONCLUSION

In this paper, we have proposed a novel hybrid method which is designed for the sparse representation of the remote sensing image. Compared with the most existing methods, the proposed method has some generality. Moreover, focus on the problem that the remote sensing image is hardly to obtain a good sparse performance if it contains a lot of details, two specialized decomposition processes are designed. Numerical results show the high validity of the hybrid method for image approximation, no matter from the subjective or objective perspective.

The limitation of the proposed method is that, the ratio of  $N_1$  and  $N_2$  is set empirically, so it may be not optimum for sparse approximation. Further researches will focus on the calculation of the ratio automatically. How to allocate the given number of coefficients properly in order to provide a good sparse appropriation while keeping the necessary details at the same time, is an issue worthy of studying. We will do some research on it in the future.

## REFERENCES

- [1] G. Plonka, S. Tenorth, and D. Rosca, “A new hybrid method for image approximation using the easy path wavelet transform,” *IEEE Trans. Image Process.*, vol. 20, no. 2, pp. 372–381, Feb. 2011.
- [2] E. J. Candes and D. L. Donoho, “New tight frames of curvelets and optimal representations of objects with piecewise  $C^2$  singularities,” *Commun. Pure Appl. Math.*, vol. 57, no. 2, pp. 219–266, 2004.
- [3] M. N. Do and M. Vetterli, “The contourlet transform: An efficient directional multiresolution image representation,” *IEEE Trans. Image Process.*, vol. 14, no. 12, pp. 2091–2106, Dec. 2005.
- [4] V. Velisavljevic, B. Beferull-Lozano, M. Vetterli, and P. L. Dragotti, “Directionlets: Anisotropic multidirectional representation with separable filtering,” *IEEE Trans. Image Process.*, vol. 15, no. 7, pp. 1916–1933, Jul. 2006.
- [5] K. Guo and D. Labate, “Optimally sparse multidimensional representation using shearlets,” *SIAM J. Math. Anal.*, vol. 39, no. 1, pp. 298–318, 2007.
- [6] G. Peyré and S. Mallat, “Discrete bandelets with geometric orthogonal filters,” in *Proc. IEEE Int. Conf. Image Process.*, 2005, pp. 65–68.
- [7] J. K. Romberg, M. B. Wakin, and R. G. Baraniuk, “Approximation and compression of piecewise smooth images using a wavelet/wedgelet geometric model,” in *Proc. IEEE Int. Conf. Image Process.*, Jan. 2003, vol. 1, pp. 1–49–1–52.
- [8] S. Dekel and D. Leviatan, “Adaptive multivariate approximation using binary space partitions and geometric wavelets,” *SIAM J. Numer. Anal.*, vol. 43, no. 2, pp. 707–732, 2005.
- [9] L. Jacques and J.-P. Antoine, “Multiselective pyramidal decomposition of images: Wavelets with adaptive angular selectivity,” *Int. J. Wavelets Multiresolut. Inf. Process.*, vol. 5, no. 5, pp. 785–814, 2007.
- [10] S. Mallat, “Geometrical grouplets,” *Appl. Comput. Harmon. Anal.*, vol. 2, pp. 161–180, 2009.



- [11] G. Plonka, "The easy path wavelet transform: A new adaptive wavelet transform for sparse representation of two-dimensional data," *Multiscale Model. Simul.*, vol. 7, no. 3, pp. 1474–1496, 2009.
- [12] C. Chuo-Ling and B. Girod, "Direction-adaptive discrete wavelet transform for image compression," *IEEE Trans. Image Process.*, vol. 16, no. 5, pp. 1289–1302, May 2007.
- [13] D. Wenpeng, W. Feng, W. Xiaolin, L. Shipeng, and H. Li, "Adaptive directional lifting-based wavelet transform for image coding," *IEEE Trans. Image Process.*, vol. 16, no. 2, pp. 416–427, Feb. 2007.
- [14] J. Krommweh, "Tetrolet transform: A new adaptive Haar wavelet algorithm for sparse image representation," *J. Vis. Commun. Image Represent.*, vol. 21, no. 4, pp. 364–374, 2010.
- [15] S. W. Golomb, *Polyominoes*. New York, NY, USA: Scribner, 1965, pp. 70–85.
- [16] I. P. Akam Bit, M. Barret, and D. Pham, "On optimal transforms in lossy compression of multicomponent images with JPEG2000," *Signal Process.*, vol. 90, pp. 759–773, 2010.
- [17] Z. Wang, A. C. Bovik, H. R. Sheikh, and E. P. Simoncelli, "Image quality assessment: From error visibility to structural similarity," *IEEE Trans. Image Process.*, vol. 13, no. 4, pp. 600–612, Apr. 2004.
- [18] J. Mathews, M. S. Nair, and L. Jo, "Modified BTC algorithm for gray scale images using max-min quantizer," in *Proc. Autom. Comput. Commun. Control Compressed Sens.*, Mar. 22–23, 2013, pp. 377–382.
- [19] CurveLab. (2008). *Curvelet Matlab Toolbox* [Online]. Available: <http://www.curvelet.org>
- [20] Minh N. Do. (2005). *Contourlet Matlab Toolbox* [Online]. Available: <http://www.ifp.illinois.edu/~minhdo/software/>



**Hao Chen** received the B.S., M.S. and Ph.D. degrees from Harbin Institute of Technology, Harbin, China, in 2001, 2003, and 2008, respectively.

He has been working with the School of Electronics and Information Engineering, Harbin Institute of Technology since 2004. His research interests include image and video compression, remote sensing imaging, and remote sensing data processing.



**Ye Zhang** (M'10) received the B.S., M.S., and Ph.D. degrees from the Harbin Institute of Technology (HIT), Harbin, China, in 1982, 1985, and 1996, respectively.

From September 1998 to September 1999, he was a Visiting Scholar with the University of Texas, San Antonio, TX, USA. Since 1985, he has been with the Department of Electrical and Communication Engineering, HIT, where he is currently a Professor with the Department of Information Engineering, School of Electronics and Information Engineering.

His research interests include hyperspectral image analysis and processing, image and video compression and transmission, and multisensor-based remote sensing image coprocessing and applications.



**Cuiping Shi** (S'13) received the B.S. degree from the Qaqing Petroleum Institute, Daqing, China, in 2004, and the M.S. degree from the Yangzhou University, Yangzhou, China, in 2007. Currently, she is pursuing the Ph.D. degree in signal and information processing from the Harbin Institute of Technology (HIT), Harbin, China.

Her research interest includes remote sensing data processing and hyperspectral image processing.



**Junping Zhang** (M'05) received the B.S. degree in biomedical engineering and instrument from Harbin Engineering University and Harbin Medical University, Harbin, China, in 1993, and the M.S. and Ph.D. degrees in signal and information processing from the Harbin Institute of Technology (HIT), Harbin, China, in 1998 and 2002, respectively.

Currently, she is a Professor with the Department of Information Engineering, School of Electronics and Information Engineering, HIT. Her research interests include hyperspectral data analysis and image processing, multisource information fusion, pattern recognition and classification.



Web of Science™

InCites™

Journal Citation Reports®

Essential Science Indicators™

EndNote™

登录

帮助

简体中文

WEB OF SCIENCE™

检索

返回检索结果

我的工具

检索历史

标记结果列表

全文选项

查找全文



保存至 EndNote online

添加到标记结果列表

第 6 条, 共 12 条

## A Novel Hybrid Method for Remote Sensing Image Approximation Using the Tetrolet Transform

作者: Shi, CP (Shi, Cuiping)<sup>[1,2]</sup>; Zhang, JP (Zhang, Junping)<sup>[1]</sup>; Chen, H (Chen, Hao)<sup>[1]</sup>; Zhang, Y (Zhang, Ye)<sup>[1]</sup>

IEEE JOURNAL OF SELECTED TOPICS IN APPLIED EARTH OBSERVATIONS AND REMOTE SENSING

卷: 7 期: 12 页: 4949-4959 特刊: SI

DOI: 10.1109/JSTARS.2014.2319304

出版年: DEC 2014

查看期刊信息

### 摘要

Most existing image sparse approximation methods can reach their best performance only under the condition that the image has some certain properties. In addition, for the remote sensing image, it is difficult to obtain a good sparse result if it contains a lot of details. Focused on the two problems, in this paper, a novel hybrid method that is of some generality is proposed. The method exploits the advantages of the tensor product wavelet transform for representation of smooth images and the ability of the tetrolet transform to represent texture and edge effectively at the same time. Moreover, two specialized processes of decomposition are designed, which contribute to increasing the energy concentration further and preserving the information of the details as much as possible. The procedure of the proposed hybrid method is as follows: for a given remote sensing image, first, the usual tensor product wavelet transform is used, then the redundancy among adjacent wavelet coefficients is removed by making a polyphase decomposition to each subband with a p-fold filter, and after that, the approximation of the low frequency image can be obtained by reconstructing those preserved coefficients. Second, for the detailed image, the sparse decomposition is carried out by the tetrolet transform. For the high frequency subbands, an adaptive decomposition will be done for increasing the energy aggregation. After that, the approximation of the detailed image can be obtained by reconstructing those preserved coefficients. Numerical results indicate the high effectiveness of the procedure for remote sensing image sparse approximation.

### 关键词

作者关键词: Remote sensing image approximation; sparse representation; tensor product wavelet; tetrolet transform

KeyWords Plus: PATH WAVELET TRANSFORM; REPRESENTATION

### 作者信息

通讯作者地址: Zhang, JP (通讯作者)

+ Harbin Inst Technol, Dept Informat Engrn, Harbin 150001, Peoples R China

地址:

+ [1] Harbin Inst Technol, Dept Informat Engrn, Harbin 150001, Peoples R China

[2] Qiqihar Univ, Dept Commun Engrn, Qiqihar 161000, Peoples R China

电子邮件地址: scp1980@126.com; zhangjp@hit.edu.cn; hit\_hao@hit.edu.cn; zhye@hit.edu.cn

### 基金资助致谢

基金资助机构

授权号

National Natural Science Foundation of China

41301455

61271348

863 High Technology Program of China

2012AA12A405

young teachers scientific research projects of Qiqihar university

2011 k-M11

查看基金资助信息

### 引文网络

#### 0 被引频次

20 引用的参考文献

查看 Related Records

查看引证关系图

创建引文跟踪

(取自来自 Web of Science™ 核心合集)

#### 全部被引频次计数

0 / 所有数据库

0 / Web of Science 核心合集

0 / BIOSIS Citation Index

0 / 中国科学引文数据库

0 / Data Citation Index

0 / Russian Science Citation Index

0 / ScELO Citation Index

#### 使用次数

最近 180 天: 0

2013 年至今: 2

进一步了解

#### 此记录来自:

Web of Science™ 核心合集

#### 建议修正

如果希望提高此记录中数据的质量, 请提供修正建议。

**出版商**

IEEE-INST ELECTRICAL ELECTRONICS ENGINEERS INC, 445 HOES LANE, PISCATAWAY, NJ  
08855-4141 USA

**类别 / 分类**

研究方向: Engineering; Physical Geography; Remote Sensing; Imaging Science & Photographic Technology

Web of Science 类别: Engineering, Electrical & Electronic; Geography, Physical; Remote Sensing; Imaging Science & Photographic Technology

**文献信息**

文献类型: Article

语种: English

入藏号: WOS:000348372000031

ISSN: 1939-1404

eISSN: 2151-1535

**期刊信息**

Impact Factor (影响因子): Journal Citation Reports®

**其他信息**

IDS 号: AZ7BA

Web of Science 核心合集中的 "引用的参考文献": 20

Web of Science 核心合集中的 "被引频次": 0



第 6 条, 共 12 条